communications earth & environment

Article

A Nature Portfolio journal

https://doi.org/10.1038/s43247-025-02378-y

X-Ray micro-tomography unveils the internal features of volcanic ash aggregates

Check for updates

Pietro Gabellini [1] ✉, Eduardo Rossi [2], Raffaello Cioni [1], Marco Pistolesi [3], Lukas P. Baumgartner [4] & Costanza Bonadonna [2]

Volcanic ash aggregation occurs during transport in the atmosphere when individual ash particles collide and stick together. It significantly impacts ash residence time in the atmosphere, with major consequences for hazard assessment and ash dispersal forecasts. Nonetheless, aggregation processes are still not adequately parametrized, mostly due to the low preservation potential of most aggregate types. We present here the first, detailed structural and morphological characterization of the major aggregate types, combining an innovative field collection strategy, which allows for the original aggregate structure to be preserved at deposition, coupled to X-Ray micro-tomography. Resulting observations together with weather information, allowed for the structure of fragile ash clusters and of the elusive cored Ash Pellets (cAP1s) to be fully resolved and their genesis to be better described. The collected dataset represents a fundamental advancement towards a comprehensive characterization of the principal aggregate categories, which is key to accurately interpreting and modelling the process of volcanic ash aggregation and dispersal.

The importance of volcanic ash aggregates

Explosive volcanic eruptions inject large amounts of tephra into the atmosphere that are transported long distances by wind advection and atmospheric diffusion. Characteristics of tephra fallout strongly depend on several factors, including plume and atmospheric conditions, aerodynamical and physical properties of the particles, and size-selective sedimentation processes (e.g., ash aggregation, gravitational instabilities[1]). Volcanic ash aggregates are the result of multiple collisions, electrostatic attraction and sticking processes of single ash particles that agglomerate during transport to create larger clusters of variable composition, size (from a few microns to a few millimeters) and shape[2–5]. While the density of aggregating ash fragments typically ranges between the bulk magma density (2.3–2.7 g/cm^3) and the density of vesicular pyroclasts (0.5–1.5 g/cm^3), resulting aggregates show a wider range of densities (0.1–2.5 g/cm^3)[6–8] depending on packing conditions. Density and size control the terminal settling velocity of ash aggregates and, therefore, their sedimentation dynamics and their residence time in the atmosphere. Fine ash (particles <63 microns) scavenged by large particle clusters typically increases its terminal velocity[4,9–11] while coarse ash and lapilli surrounded by a fine-ash shell might decrease their terminal velocity because of an increase in their drag coefficient (the so-called *rafting effect*[12]). Given the complexity of sedimentation dynamics, it is of fundamental importance to increase our capability to fully characterize ash aggregates and their airborne internal structures to accurately perform ash-dispersal forecasting[13]. According to recent classification schemes[2,9], volcanic aggregates can be classified in two main categories: (i) accretionary pellets (APs), including poorly structured sub-spherical clusters (AP1), pellets with concentric structures (AP2), and liquid pellets (AP3); (ii) particle clusters (PCs), including irregular ash clusters between particles of roughly the same size (PC1), coated particles with a large core and a thin coating (PC2), and cored clusters with a large central core enclosed by a thick shell of fine ash (PC3).

Volcanic ash aggregates have a generally low preservation potential as they typically disaggregate upon impact with the ground[2,9]. This is primarily due to the high energy of the impact, compared to the weak adhesive and cohesive (liquid water and ice) forces and electrostatic bonds that hold individual constituents together, especially inside PCs[6,11,14–16]. Important insights into the structure and grain size of fragile APs and PCs have been obtained via in-situ collection of samples on adhesive tapes, later analyzed with the Scanning Electron Microscope (SEM)[8,17,18]. Additional information on cluster density and settling velocity has been derived from high-speed camera observations[7,19], while the combination of adhesive-tape collection and high-speed camera footage provided a better characterization of individual APs and PCs categories[8,9,20]. Nonetheless, due to their fragility and their elusive and occasional occurrence (often under extreme logistical

[1]Department of Earth Sciences, University of Florence, Florence, Italy. [2]Department of Earth Sciences, University of Geneva, Geneva, Switzerland. [3]Department of Earth Sciences, University of Pisa, Pisa, Italy. [4]Institut of Earth Sciences, University of Lausanne, Lausanne, Switzerland. ✉e-mail: pietro.gabellini@unifi.it

conditions such as heavy ash fallout), investigating the internal structure of specific aggregate types, especially AP1, PC1, and PC3, turns out to be very challenging or even impossible. An exception is represented by the AP2 aggregates (also defined accretionary lapilli in literature), generally well preserved in deposits thanks to their high overall mechanical strength and rigid habit given by their matrix-supported structure[2] and the presence of binding salt [21]. Their formation is related to specific plume mixture conditions, which probably involve water, salty aerosol, and high temperature[22–27].

A new strategy for studying volcanic ash aggregates

In this study, we present the first detailed information on the internal structure of the most fragile volcanic aggregates thanks to the ad-hoc combination of a new state-of-the-art field sampling strategy, involving the coupled use of ultra-violet (UV) sensitive resins and HR-HS cameras (HSC), with laboratory analysis based on the use of high-resolution X-Ray micro-Computed Tomography (μCT). The combination of UV resins and HSC allows for the preservation of the original airborne structure of the aggregates and for the determination of their settling velocity. The use of μCT guarantees access to the inner structure with a high-resolution and non-invasive approach for the sample. During collection, we used a thin layer of UV resin on a glass support to dampen the impact of the falling aggregate and prevent the collapse of its delicate airborne structures. Aggregate fall was also recorded by an HSC to guarantee that no modifications (breakage, rebound) occurred during ground sedimentation (Fig. 1; see Section S2 of supplementary materials and Supplementary Movie 1 in the online repository). Just after landing, the aggregate was then fully covered with additional UV-sensitive resin, if needed, and hardened by a UV-light source. Finally, the embedded sample (ash aggregate and UV resin) was analyzed using the μCT to provide a 3D tomographic reconstruction of the internal structure and of the spatial distribution of the single ash constituents.

The μCT is used as a diagnostic device in medical applications, for the internal reconstruction of disparate objects in the industry[28] and in earth sciences to look at mineral and fossil structures[29]. Several studies have applied μCT scanning to the investigation of single ash and lapilli particles[30] and AP2 aggregates (i.e., accretionary lapilli), which are typically found well preserved in the deposits[26]. However, thanks to the proposed sampling technique and the high-resolution of our μCT instrument (~ 4.2 μm), the present work represents the first application of X-ray micro-tomography to a wide set of different aggregate types, particularly the most fragile and elusive ones (PCs and APs). The analyzed samples were collected during ash-dominated Vulcanian eruptions that occurred at Sakurajima volcano (Japan) in November 2019. The dataset presented here includes PC1, PC2, PC3, AP1, AP3 and some newly observed hybrid samples, hereafter called "*cored AP1*" (cAP1). Meteorological conditions during aggregate settling were also monitored during field sampling (Table 1), to discuss possible relations with aggregate types and variable atmospheric conditions. In a complementary paper, Vecino et al.[20] showed the significant influence of meteorological conditions on aggregate speciation, highlighting in particular the role of air moisture or liquid water (i.e., rain) in controlling the occurrence of AP aggregates. The relationship between meteorological conditions and aerodynamical features of the different aggregates is of high interest for the present study since it facilitates the interpretation of the structural and morphological information observed using μCT analysis.

The X-ray tomography of aggregates with size of a few hundred microns required an accurate calibration of the resulting images, which has been achieved by defining a calibration curve based on measured standard materials with known densities and volumes. In addition, a semi-automatic MATLAB algorithm has been specifically designed for the post-processing of the tomographic images (see on-line Methods). As a result, here we show the first comprehensive dataset of high-resolution, 3D renderings of both the external morphology and the internal structure of a variety of natural, well preserved PCs and APs aggregates. Several fundamental physical quantities were measured thanks to the tomographic images and the post-processing analysis (i.e., volume of the original aggregate, bulk density,

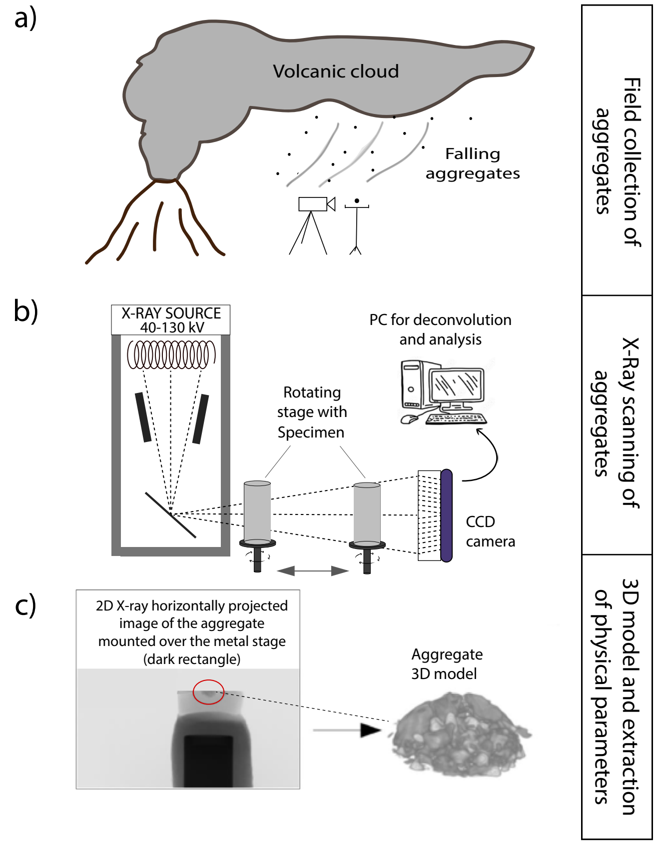

Fig. 1 | Schematic representation of field sampling and laboratory analysis adopted in this work. a In-situ sampling of ash aggregates; **b** working principle of a μCT: X-rays are generated in an X-ray source at a constant voltage. The best images were obtained with a voltage of 50 kV. The x-rays passed through the sample to the CCD detector as a 2D projection image. The sample is rotated on the stage in steps. For each step on several X-ray projection images are taken. Step size depends on the resolution required (down to fraction of degree). The resolution (pixel size) is a function of the distance between x-ray source and the CCD camera, the pixel size, as well as the X-ray generation spot. The series of X-ray projection images (**c**) is then computed into cross-sectional images through the computational process called "reconstruction". These slices can be analyzed and processed to produce 3D models of the aggregates.

porosity, and mass distribution). In addition, the inner lithology and the internal arrangement of the single particles were visualized by means of scaled 3D renderings.

Our high-resolution images aim to set a new standard for classification, quantitative descriptions and theoretical studies of the most common ash aggregates associated with volcanic plumes and volcanic clouds[2,9].

Aggregate formation is generally driven by collisional and sticking processes, in their turn influenced by particle size, relative particles velocity, and dissipative mechanisms[4]. We also know that ash aggregation depends on factors like particle-turbulence interactions, electrostatic charges, liquid layers, and particles concentration. However, all these scenarios remain limited due to the lack of a detailed, complete, and unbiased benchmark of how the internal structure of aggregates is organized by natural and not easily reproducible processes, especially for what concerns fragile and poorly preserved structures. The presented dataset fills a crucial gap, offering a detailed look at the naturally complex internal structure of aggregates, which embodies their entire formation history.

Results

Field conditions and observations

A large set of HSC videos of aggregates landing on UV-sensitive resin was collected. This sampling approach allowed us to entirely preserve the

Table 1 | Features of eruptive parameters, weather and atmospheric conditions recorded at the different sampling locations (see also ref. 20) for each aggregate

ID	Type	Sampling Location	Distance from vent		Eruption onset timing	Time of collection	Plume height	Atmospheric and weather conditions		
–	–	[Lat° Lon°]	GPS code	km	{JST}	{JST}	m (a.s.l.)	T (°C)	RH (%)	Sky conditions
TT_2100	PC1	31.622972; 130.660167	L3	4.5	2019-11-17 [13:52]	14:09	3300	22.8	61.6	Clear sky
TT_2107	PC1	31.619222; 130.689528	L6	4.9	2019-11-26 [14:24]	NA	3700	18.8	73.0	Rainy
TT_2109	PC2	31.589761; 130.601038	L5	5.2	2019-11-23 [16:11]	16:25	2200	20.9	75.6	Cloudy
TT_2140	PC2	31.589761; 130.601038	L5	5.2	2019-11-17 [11:12]	11:40	1780	22.8	61.6	Clear sky
TT_2118	PC3	31.619222; 130.689528	L6	4.9	2019-11-26 [14:24]	NA	3700	18.8	73.0	Rainy
TT_2126	PC3	31.589761; 130.601038	L5	5.2	2019-11-23 [14:20]	14.28	3100	21.3	75.2	Cloudy
TT_2153	AP1	31.589761; 130.601038	L5	5.2	2019-11-23 [14:20]	14.33	3100	21.3	75.2	Rainy
TT_2129	AP1	31.589761; 130.601038	L5	5.2	2019-11-23 [14:20]	14.33	3100	21.3	75.2	Rainy
TT_2111	cAP1	31.589761; 130.601038	L5	5.2	2019-11-23 [14:20]	14.33	3100	21.3	75.2	Rainy
TT_2127	cAP1	31.589761; 130.601038	L5	5.2	2019-11-23 [16:11]	16:31	2200	20.9	75.6	Rainy
TT_2133	AP3	31.619222; 130.689528	L6	4.9	2019-11-26 [14:24]	NA	3700	18.8	73.0	Rainy
TT_2137	AP3	31.619222; 130.689528	L6	4.9	2019-11-26 [14:24]	NA	3700	18.8	73.0	Rainy

The plume height and the timing of the eruption onset are also reported in Japan Standard Time (JST). The GPS location of the collection spot and its position label are shown here, according to Fig. 1 in ref. 20. The atmospheric Temperature (T) and the Relative Humidity (RH) measured at ground level are shown in the last column of the table with the sky condition observed during sampling.

airborne structures of the large majority (more than 90%) of the observed aggregates (see Section S2 of supplementary materials for details).

The dataset consists of 51 aggregates and includes the principal aggregate types observed during previous field works at Sakurajima volcano, and other volcanoes[2,7–9,17,18,20,31]: PC1, PC2, PC3, AP1, and AP3. We also identify an additional type of poorly structured pellets with larger internal particles (one or more) acting as nuclei[2], here named as cAP1 to distinguish them from classical AP1, normally occurring without an internal core. Only internally structured pellets (accretionary lapilli, AP2) were not observed in our dataset. The studied samples show the potential of X-Ray tomography in discriminating the presence and quantifying the abundance of different aggregate types and particularly of the cAP1s in ash fallout. In fact, based only on the external morphology, cAP1 are not easily distinguishable from normal AP1.

Table 1 shows the details of the eruptive activity, the sampling and the weather conditions associated with the aggregates selected for this work. The selection of 12 samples from the dataset is made in order to illustrate the end-members of the structural and morphological variability existing within each category.

The eruptive activity of Sakurajima during sampling was characterized by sudden variations in the style and intensity of ash emission, well in accord with the classical pattern representing the most recent, long-lasting activity period which started in 1955[8,32,33]. Activity was characterized by a persistent, low-intensity ash emission forming weak plumes, laterally displaced by wind and associated with modest proximal sedimentation. This background ash emission was occasionally punctuated by sudden and violent Vulcanian explosions, which injected into the atmosphere considerable amounts of ash in the form of strong plumes that vertically rose up to a maximum height of 3700 m a.s.l. A detailed description is reported in Section S1 of the Supplementary Materials.

All aggregates were collected at distances of 4.5–5.2 km from the vent, under the dispersal axis of Vulcanian plumes of comparable intensity (plume heights from 1780 to 3700 m asl). While tephra fallout was often characterized by the simultaneous sedimentation of multiple aggregate categories (e.g., Table S4), some aggregate types better correlate with meteorological conditions than others (Fig. S8)[20]. PC3s were observed to primarily occur in clear sky conditions, while APs are specific of high-humidity and rainy conditions (Fig. S8 and Table S4). In particular, the cAP1 and AP3 were identified only in the presence of high-humidity conditions (i.e., cloudy and rainy conditions), suggesting a key role of raindrops in controlling the binding mechanism (Tables 1, S4, and Fig. S8). On the other hand, PC1 and PC2 show a poor correlation with local atmospheric conditions, suggesting binding mechanisms mostly controlled by intra-conduit and/or intra-plume particle-particle interaction, as the case of triboemission and fractoemission processes. These mechanisms promote the superficial electrostatic charging of ash particles within high-concentrated regions of the conduit and plume, and, therefore, they are independent on atmospheric conditions[34–36].

External morphology of aggregates

A major result of X-ray tomography applied to the study of volcanic aggregates is represented by the 3D rendering of the external surface of each aggregate type (Fig. 2). This was achieved by means of two different representations: Stereolithographic (STL) models, where the external surface of the greyscale volume renderings is discretized in triangles and classically used for 3D printing (Fig. 2b, d), and volumetric renderings, where each voxel is given a color (depending on the voxel value or grayscale level) and an opacity in order to visualize the μCT results as a 3D volumetric rendering (Fig. 2a, c).

The obtained STL models (Fig. 2b, d and Table 2; see.STL files in the online repository) allowed us to characterize key features of the aggregates' morphology, such as shape and external surface roughness. Moreover, this approach opens the path to the use of high-quality and high-resolution 3D printing for analog simulations and experiments aimed, for example, at evaluating the influence of specific morphologies on aggregate sedimentation.

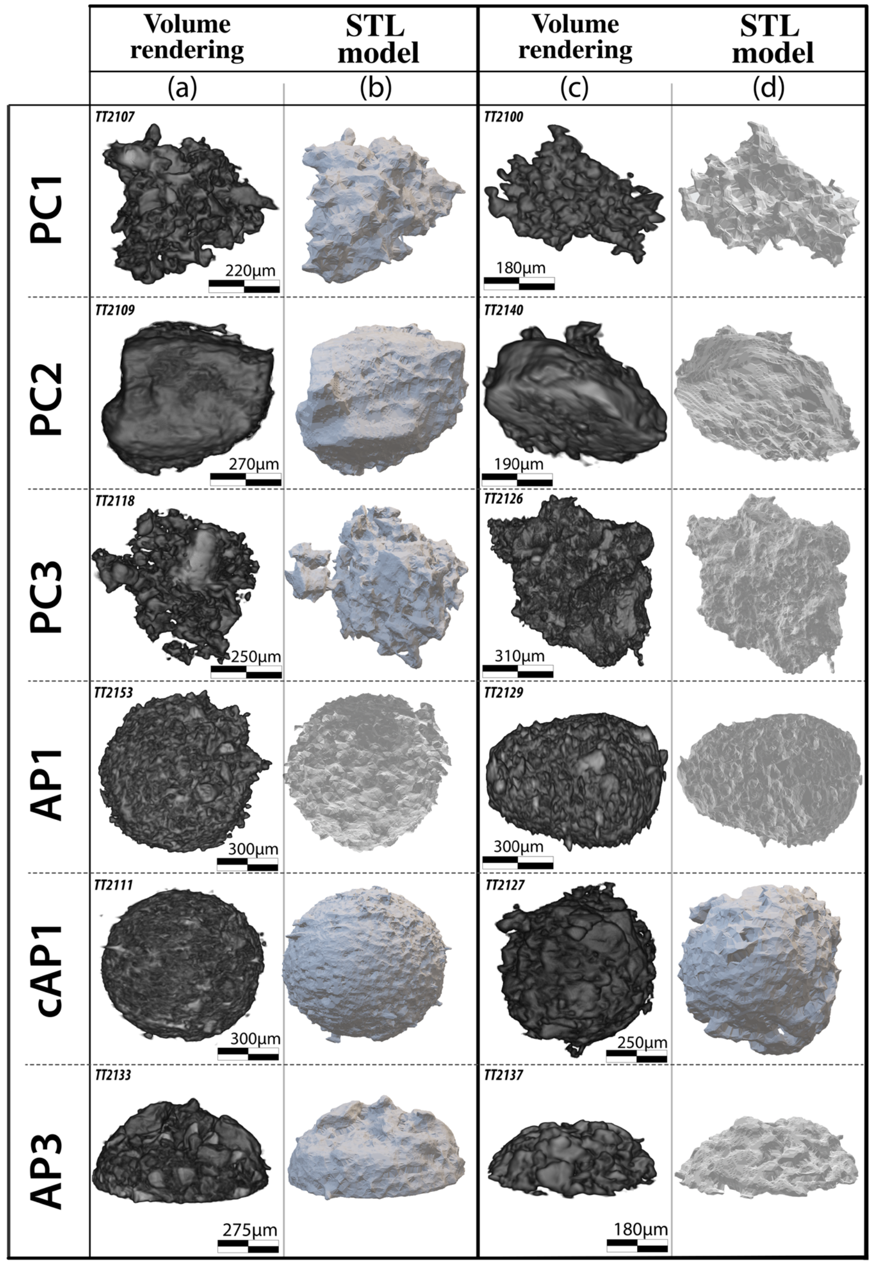

Fig. 2 | External morphologies of aggregates. Volume (**a**, **c**) and stereolithographic (**b**, **d**; STL model) renderings of two selected aggregates for each aggregate category. These 3D renderings were obtained using a dedicated MatLab routine (see the on-line materials for further details). Downloads of the associated STL files are available in the on-line repository.

3D shape parameters calculated for aggregates shown in Fig. 2 and for all the aggregates considered in this study are presented in Table 2 and Fig. S9, respectively (see Section S5 of Supplementary Materials and on-line methods for further details and definition about used shape indexes). The value of Surface Roughness, an index introduced in this study and used to quantify the roughness of the external aggregate surface (Eq. S5.4), is also reported in Table 2 for each aggregate type.

In addition, the volumetric renderings (Fig. 2a, c) provide complementary information to STL models. They allow the unbiased visualization of the external aggregates' morphology with details on the spatial arrangement of particles forming the external surface.

The different types of aggregates are characterized by specific shape parameters (Fig. 2). In general, the external shape of Particle Clusters (PCs) is characterized by several lobes and asperities which result in a higher irregularity compared to the smoother and more equant morphologies of the APs (Fig. 2 and Table 2). This is also confirmed by the lower values of Sphericity and Solidity (respectively "S", the ratio between the surface area of a sphere with the same volume as the given aggregate and its external surface (Eq. S5.3), and "SLD", the ratio of the aggregate volume to the volume of its convex hull (Eq. S5.1)) showed by PCs compared to APs (respectively blue, red and yellow colored areas and violet, green and light blue areas in Fig. S9).

A thick and pervasive layer of fine particles characterizes the external surface of both PC1 and PC3, which makes these aggregates very difficult to be distinguished if only the external surface is analyzed. Both PC1 and PC3 show highly complex external morphologies, which are strongly influenced by grain size, thickness, and specific architecture of this fine-ash shell of aggregating particles. The similar external aspect (Fig. 2a–c) also yields to a similar global shape, as indicated by converging S values resulting in the partially overlapping of blue and yellow areas in Fig. S9). The presence of diffuse asperities and pronounced lobes on the outer perimeter (Fig. 2) produce a rough and convoluted external surface, marked by very high degree of Surface Roughness, between 42 and 64% (Table 2) and by SLD values always below 0.7 (Fig. S9). The slight morphological difference between PC1 and PC3 is well represented by variable S and Convexity values ("CVX", the surface of the convex hull to the surface of the aggregate—Eq. S5.2 and Fig. S9b), respectively comprised between 0.7 and 0.85 and 0.25

Table 2 | Physical parameters calculated for aggregates reported in Fig. 2

Sample ID		Internal Structure						External Features				
ID	Type	Size	Density	Porosity	Internal Components volume fraction (%)			Core Size	Surf. Rough.	3D Shape parameters		
–	–	μm	g/cm³	Vol.(%)	*Low density*	*Int. density*	*High density*	μm	(%)	S	SLD	CVX
TT_2100	PC1	331 [267; 352]	2.69 [2.19; 2.70]	11.0 [8.1; 16.2]	75	24	1	Not present	61	0.783	0.369	0.587
TT_2107	PC1	618 [534; 687]	2.76 [2.42; 2.76]	12.5 [10.2; 15.5]	62	35	3	Not present	53	0.723	0.463	0.693
TT_2109	PC2	466 [451; 485]	2.95 [2.81; 2.95]	0.4 [0.3; 0.5]	39	61	0	455 [440; 473]	19	0.853	0.807	0.984
TT_2140	PC2	372 [352; 389]	3.76 [3.70; 3.76]	0.4 [0.3; 0.6]	23	21	56	360 [340; 376]	25	0.829	0.731	0.808
TT_2118	PC3	615 [478; 681]	3.07 [2.85; 3.07]	10.0 [8.7; 11.0]	53	28	18	273 [212; 302]	64	0.728	0.343	0.514
TT_2126	PC3	859 [788; 949]	2.82 [2.55; 2.82]	1.1 [0.8; 1.8]	62	36	2	336 [309-; 371]	42	0.725	0.571	0.520
TT_2153	AP1	836 [793; 861]	2.74 [2.23; 2.76]	1.3 [0.9; 3.4]	62	35	3	Not present	21	0.900	0.781	0.658
TT_2129	AP1	721 [696; 738]	2.88 [2.58; 2.89]	2.8 [3.2; 3.8]	59	35	6	Not present	16	0.907	0.833	0.597
TT_2111	cAP1	826 [799; 839]	2.86 [2.58; 2.87]	0.8 [0.5; 1.8]	63	34	3	397 [384; 402]	13	0.946	0.861	0.416
TT_2127	cAP1	553 [514; 573]	2.82 [2.53; 2.83]	1.8 [1.6; 2.2]	59	40	2	252 [234; 261]	27	0.889	0.719	0.720
TT_2133	AP3	712 [678; 742]	2.86 [2.59; 2.86]	7.8 [6.9; 8.5]	49	45	6	Not present	23	0.737	0.761	0.701
TT_2137	AP3	367 [326; 376]	2.89 [2.73; 2.89]	2.6 [1.5; 4.6]	63	35	2	Not present	32	0.631	0.636	0.539

Values are listed together with their associated uncertainties, respectively (minimum and maximum values are reported in square brackets). Confidence intervals were estimated according to methods reported in the on-line repository. The Aggregate and Core size (were present) are expressed as the sphere equivalent diameter. Dimensionless shape parameters [Sphericity (S), Solidity (SLD), and Convexity (CVX)] reported in the last columns are defined according to refs. 50–52.

and 1. This indicates that PC1 are characterized by higher irregularity (e.g., TT2100 in Table 2) compared to PC3 (e.g., TT2126 in Table 2). These morphological characteristics well agree with the pronounced fragility shown by these aggregates.

On the contrary, PC2 aggregates are characterized by a thin, sometimes discontinuous coating of fine ash (< 63 μm), which results in a generally smoother external surface (Fig. 2) as also indicated by the lower values of Surface Roughness (Table 2) and higher CVX. The shape of PC2 is, therefore, essentially controlled by the morphology of the large single particle (Fig. 2) rather than by the features of the coating ash. In fact, PC2s show the highest values of SLD among Particle Clusters (Fig. S9a, b) indicating a blocky global form reflecting the typical shape of ash particles produced during Sakurajima's recent activity[37].

Finally, Accretionary Pellets (APs) are characterized by less variable and more equant external morphologies (Fig. 2). These aggregates vary from a typical spherical shape for AP1s and cAP1s, to a characteristic hemispheric shape in the case of AP3s (Fig. 2b–d), resulting in a high value of SLD (between 0.6 and 0.9; Fig. S9). S is also very high ($S > 0.85$) in all the observed aggregates (Table 2; Fig. S9) except for AP3s, whose S values are comprised between 0.631 and 0.737 due to their characteristic hemispheric shape. The external surface of all the APs is in general smoother than those of the PCs, as indicated by the very low values of Surface Roughness, always between 13 and 32% (Table 2). However, the number of small-scale asperities is generally higher as suggested by the low CVX values (<0.7), possibly due to the lower grain size which generally characterize these aggregates.

Internal structure of aggregates and density mapping

A multi-level segmentation approach was used to reconstruct the internal regions of the aggregates and obtain a model with different iso-density levels. The raw gray-scale tomographic reconstruction (i.e., volume renderings) is shown together with the maximum intensity projection (MIP) images, and the spatial distribution of density and porosity (Fig. 3). The main physical parameters were also estimated for the different aggregates: size, density, porosity, relative volume of internal components and, when present, the core size (Table 2).

In general, both PCs and APs are made of a polydisperse size distribution of particles characterized by variable density and lithology (Fig. 3a, b). On the other hand, the specific architecture of the internal constituents and their grain size vary according to the aggregate type (Fig. 3). PC2s are characterized by the presence of sparse and small clasts forming a discontinuous layer around a large particle, which generally represents more than 90 vol.% of the aggregate volume (Table 2). The morphology of this large particle strongly controls the general shape of the aggregate (Fig. 3a). Conversely, PC1s consist of a polydisperse distribution of fine-to-coarse ash particles (generally below 50–100 μm) with no apparent arrangement of the internal constituents (Fig. 3a). Finally, PC3s display a well-organized arrangement of the internal constituents, characterized by the presence of a large, massive core particle in the central position surrounded by an ash shell of variable thickness. In the observed PC3s the core represents a small volumetric fraction of the whole aggregate (around 8–10 vol.%; Fig. 3 and Table 2) and is totally coated by a thick ash shell made of particles finer than 100 μm. No evident spatial and dimensional organization (e.g., iso-oriented clast or regular bedding geometries) were revealed in the coating shell of PC3s (Fig. 3).

According to ref. 2, Ash Pellets do not show an organized structure of their internal constituents, except for the AP2 type (not observed in the present study). This is also confirmed by the tomographic images, in which particles of variable size and lithology are distributed all around the aggregates (Fig. 3). However, cAP1 clearly show a massive core (around 10 vol.%; Fig. 3) at the center of the aggregate that is totally covered by finer particles, similarly to what is observed for PC3 aggregates. Interestingly, the cAP1 are indiscernible from normal AP1 based solely on their external appearance (Fig. 2). In this case, as also observed for PC3s, the detail on the internal structure is crucial for a correct aggregate identification.

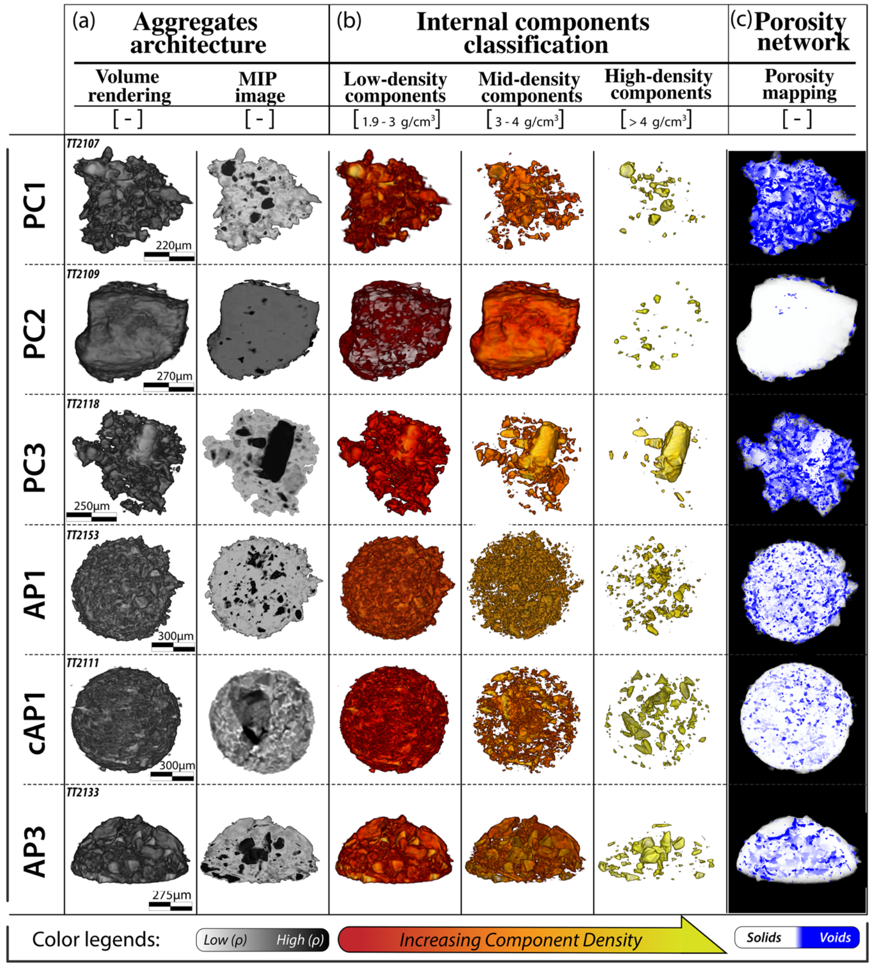

Fig. 3 | Internal structure of aggregates. 3D volume rendering of each aggregate (**a**) is reported close to the 3D Maximum Intensity Projection image (MIP) with inverted greyscale in order to display the spatial arrangement of internal components (**b**). In these density calibrated images the color bar is scaled according to single voxels density and the darker the pixels the denser is the constituent; (**b**) 3D rendering of the internal architecture of the components matching three different density intervals (Low-density, Mid-density, High-density) which corresponds with the typical density of Glass-Feldspars (1.9–3 g/cm^3), Mg-Olivine (3–4 g/cm^3) Fe-Ti Oxides (>4 g/cm^3) (**c**) 3D mapping of porosity frameworks calculated for the different aggregate categories showing the spatial distribution and the exact position of voids within the aggregate. Images were obtained applying an appropriate degree of opacity and white color to the solid particles and showing the voxels network representing internal voids as blue opaque.

Porosity network of the ash aggregates

The original geometry of the porosity network of the analyzed aggregates was reconstructed based on the internal density mapping (Fig. 3c). Values of bulk porosity are reported in Tables 2 and S4 for each aggregate. Both the relative volume fraction of pores (porosity) and their 3D spatial distribution are highly variable and correlate with aggregate category (Fig. 3c). PC2s show a very low porosity, generally lower than 1 vol.% (Table 2), and entirely localized in external ash rim. The volume fraction of voids is significantly higher in PC1s and PC3s (around 13 and 16 vol.%, respectively; Table 2). In PC1s the porosity forms an interconnected network of pores that pervasively extends through the entire aggregate without apparent internal organization (Fig. 3c). In PC3s, pores are confined to the external shell, thus highlighting the presence of a dense core located in the center of the aggregate.

Ash pellets (AP1s, cAP1s, and AP3s) show lower porosity than PCs (Fig. 3c), which ranges between a few percent to 20 vol.% in AP1s and cored-AP1s, respectively, while it reaches values up to 27 vol.% in AP3s (Table 2). In the case of AP1s and cAP1s, the porosity forms a disconnected framework composed of small and sparse voids homogeneously distributed through the 3D volume of the aggregates (Fig. 3c). AP3s display a slightly more interconnected network of voids which is characterized by slightly bigger pores that are localized in the close vicinity of the larger clasts.

Discussion

Quantification of physical parameters using μCT: pros and cons

The derived calibration curve allowed us to establish objective density threshold limits for the aggregate constituents from the X-ray tomographies and, therefore, to quantify several parameters including aggregate porosity based on CT data (Fig. 3c and Table 2). The derived parameters allow the identification of some important trends, providing insights into aggregation mechanisms. Moreover, this approach represents the only method currently available to quantify the porosity of the most fragile aggregates categories (PCs, AP1s, and AP3s). It is worth noticing that this information was previously presented in literature only for the rigid and well preserved AP2s, while the bulk density for the other aggregate categories was derived from the coupled measure of the mean aggregate size and settling velocity[7,8,19,20]. This new technique thus represents an independent method to measure the density and the porosity of all the aggregate types. In addition, the μCT analysis also allows the effective visualization of the 3D spatial distribution of the internal porosity network of the aggregates (Fig. 3c), which is an original piece of information, never obtained for the most fragile aggregate categories (PC1, PC2, and PC3)[8,9].

Other major physical parameters were also calculated, such as size and density of both the aggregates and of their internal constituents (Table 2). Information was finally derived on morphometry (Fig. 2 and Table 2) and spatial distribution of the internal constituents (Fig. 3b), providing a high-precision description of the internal structures of the aggregates. This information was used to better constrain the physical characteristics of aggregates and reveal possible general trends and fields of existence peculiar to the different aggregate types.

The aggregate density was compared with the bulk porosity and the relative volume fraction of high-density components (mostly Fe-Ti oxides), revealed thanks to the iso-density mapping reported in Fig. 3 (Fig. 4 and Table S4 of Supplementary Materials). As expected, a general inverse trend confirms that density is primarily controlled by the aggregate porosity (Fig. 4a). However, also the internal lithology can play an important role as

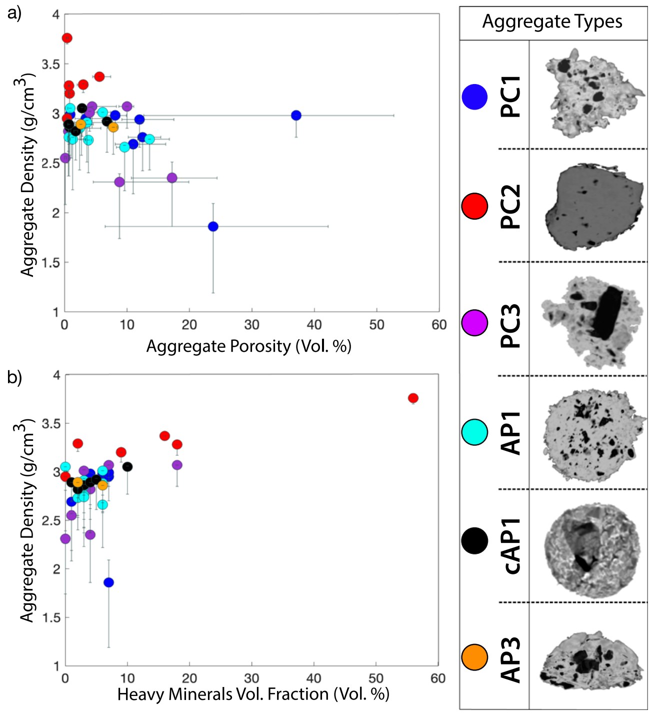

Fig. 4 | Main physical parameters extracted from calibrated tomographies. Plot of density vs porosity (**a**) and density vs relative contents of heavy minerals (high-density components) (**b**) for all the analyzed aggregates in this study. Colors refer to the different aggregate categories identified in the considered sample dataset. Visual examples of the internal structure characterizing each aggregate type are reported on the right (as MIP images).

indicated by partially misaligned particles with respect to the trend, particularly evident for PC2s and a PC3 in Fig. 4b. Conversely, the main factor controlling density for cAP1s and PC3s is related to the size and the nature of the massive core fragments. Finally, due to the presence of a coarse-grained core (around 95–97 vol.%; Fig. 4b), PC2s are characterized by the highest values of bulk density (up to 3.8 g/cm^3) and low porosity (< 10%; Fig. 4a).

APs show a limited scatter both in terms of density, which ranges between 2.3 and 3 g/cm^3, and in terms of porosity, which is very low for all the APs (only one AP1 reaches a value up to 20%). All the cAP1s display very low porosity and a density between 2.5 and 3.1 g/cm^3, which also accounts for a general limited variability of the internal lithology associated with a general higher fraction of fine components (size <63 μm).

The derived physical parameters are sometimes affected by a large uncertainty mainly due to the presence of dark artifacts in the reconstructed tomographies: these consist of dark shaded zones in the X-ray images likely caused by minimal sample motions during scanning which can occur as a consequence of sample heat up due to X-ray exposure (see Fig. S6 in supplementary materials and Methods for further details). The effect of these artifacts on the estimation of physical parameters is likely increased by the large lithological variability and morphological complexity proper of the polydisperse internal components of aggregates.

Given this considerable uncertainty affecting the dataset, the absolute values of parameters like aggregate density or derived porosity might be overestimated. This possibly justify also the presence of some outliers in our dataset (e.g., PC1 in Fig. 4a), in which both the estimated porosity and density are affected by a large uncertainty.

For all these reasons, the new data are in some cases poorly comparable with data derived with different methods from previous literature. As an example, the mean density values of PC3s in ref. 8 and in ref. 20 never exceed 1.6 g/cm^3 and 1.1 g/cm^3, respectively. Both these values are lower than the range reported here for PC3, which is between 1.7 and 2.9 g/cm^3. This inconsistency also arises for other types of aggregates (e.g., PC1 and PC2), for which the density values obtained with μCT are always about twice the values estimated using the HSC approach[8,20].

This inconsistency can be partially explained with the intrinsic uncertainty proper of the two approaches used to conduct the measurements. The two methods are, however, in part complementary in defining the range of aggregate densities. The μCT analysis possibly produces density values at their higher limit, as a consequence of a general overestimation of the volume occupied by the particles (due to the fuzzy limits of the grey-scale), and especially of the densest components (for the dark flare effect described above). On the other hand, the HSC method may result in an underestimation of the aggregate density, because of a likely overestimation of the volume of the aggregate, approximated to the convex envelope of the aggregate[7,8,20]. In this method terminal velocity and volume of the falling aggregates are in fact obtained through the measurement of the position and 2D average diameter of the projected perimeter of the aggregate, as derived from a few images of the falling aggregate[7]. Accuracy of this measure is difficult to estimate, since it is related to the complexity of shapes and to the quality in the HSC frame due to bad image focusing, which is not often easy to optimize due to the extreme working conditions and occasional presence of ash aggregates. Despite that, an approximation of the overestimate associated to the HSC method can be derived from the SLD values calculated for the aggregates (Table 2 and Fig. S9), which show that the volume of the convex envelope of an aggregate can be up to about 2.5 times larger than its real volume, especially for those aggregates with complex external morphology (PC1, PC3).

On the other hand, the accuracy of μCT analyses is mostly controlled by the resolution limit of the instrument (here is approximately 4.2 μm) and by the occasional presence of dark flares artifacts in the reconstructed tomographies associated with the denser components. However, these limits in the application of μCT do not undermine its unique capacity to provide information on the spatial distribution of porosity and density inside the aggregate volume and the 3D morphological rendering of external shape and internal structures, that are not available in the literature. Furthermore, the performed quantitative results presented in Table 2 display an overall good consistency, which agrees with the structural characteristics evidenced by the 3D imaging for the different types of aggregates.

New insights into aggregation mechanisms of APs

Particle clusters and accretionary pellets are characterized by specific and different external morphologies (Fig. 2) and internal structures (Fig. 3). This suggests different aggregation mechanisms. All the APs share a common smooth external morphology, which differs from the higher complexity of PCs. In particular, APs display very low values of Surface Roughness (Table 2) given by external surfaces varying from a sub-spherical (AP1 and cAP1; Fig. S7) to a marked hemispheric morphology (AP3). The morphologies of the APs (Fig. 2 and Table 2) show a poorly organized internal architecture (Fig. 3), suggesting the presence of a liquid phase as the main factor controlling the aggregation mechanisms. However, while the AP3s were observed to be closely related to liquid droplets while impacting on the UV resin, a more rigid structure was observed for both AP1s and cAP1s. No significant differences were shown in the magnitude and pervasiveness of the porosity network for AP aggregates that could justify a remarkable variability in the kinetics of water evaporation during settling from the plume between AP3 and other APs. As a matter of fact, the plastic behavior shown by AP3s at the moment of impact can be interpreted as the difference in the source origin rather than a difference in the aggregation mechanism. For these aggregates, data suggest a genesis controlled by the direct interaction with rain droplets occurring sufficiently close to the ground to preserve water as a liquid phase. This is consistent with meteorological observations carried out during sampling, which highlight the occurrence of AP3 only during rainfalls and, on the other hand inform about the occurrence of PC3 only during dry atmospheric conditions (Fig. S8 and Table S4).

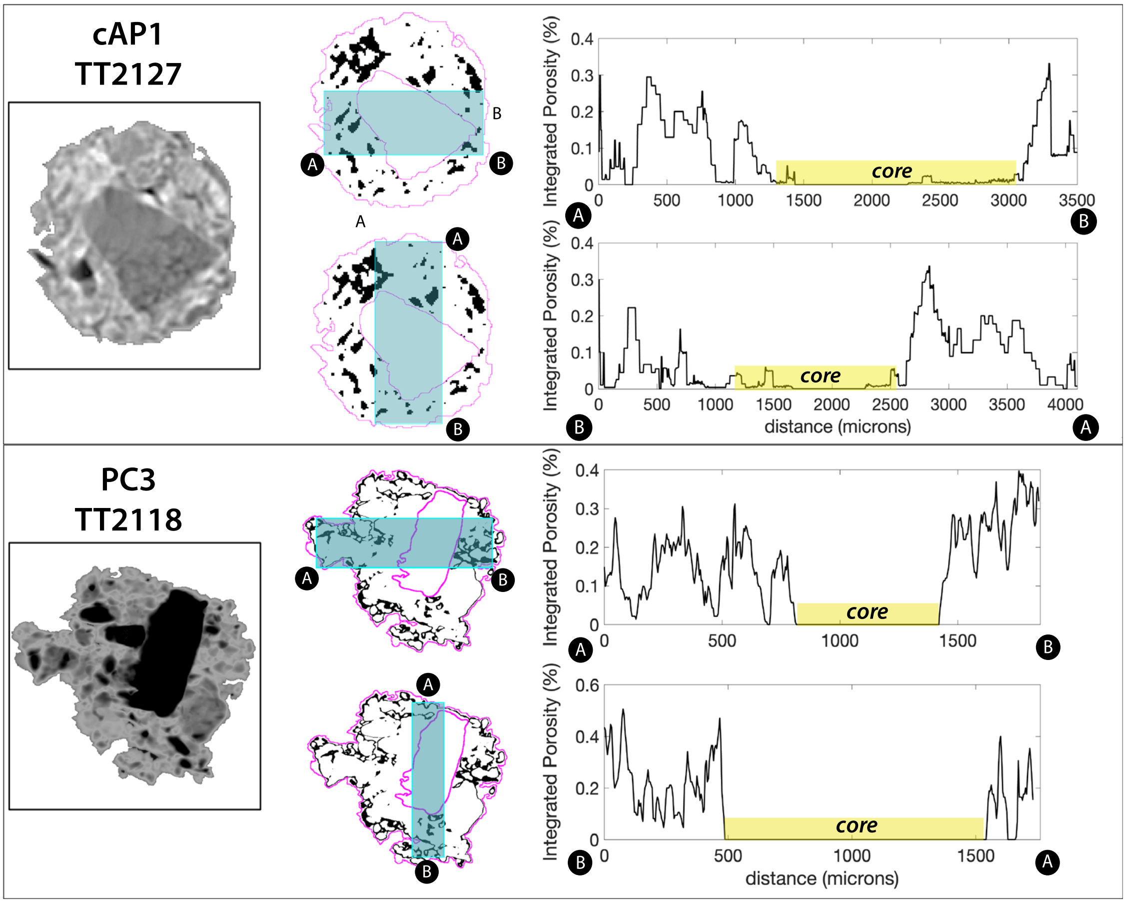

Fig. 5 | Radial distribution of porosity in the shell of PC3s and cored-AP1s. Profile plot show the spatial variability of porosity calculated across the horizontal and vertical profiles (rectangular shaded profiles) traced along a random 2D cross section of the aggregate. Corresponding images were segmented based on the computed calibration and local porosity (black pixels) was calculated based on the measured greyscale value across horizontal and vertical profiles.

AP2s is the only aggregate category that has never been observed during this type of volcanic activity at Sakurajima[8,9,20,23,31,38]. In fact, AP2s are indeed typically associated with water-rich eruptions, often involving pyroclastic density currents[3,24,27,39] in which humidity and temperature can reach higher values, and turbulence is much more intense than what observed in Sakurajima activity.

Another important result of the application of the μCT analysis is the accurate description of the cAP1 with internal larger particles acting as a nucleus. In fact, the 3D imaging of the aggregate structures confirms the presence of a core in some AP1, a possibility already suggested by ref. 2. Given the non-distinctive external features, cAP1 could not be easily identified without MicroCT imaging. Structural details on the architecture of cAP1 suggest a specific mechanism of formation. Despite the different external shape with respect to PC3, their similarities in the internal structure (i.e., presence of a large core surrounded by a shell of fine to coarse ash with no visible gradient in grain size) together with the exclusive occurrence of cAP1 during rainy conditions (Table 1), suggest a formation process possibly related to the interaction of PC3s with water droplets. This supports the idea that most of the collisions between large and small particles - that trigger the formation of PC3 type aggregates - occur inside the volcanic plume, chronologically before the interaction with atmospheric water droplets. Conversely, pure AP1s (i.e., without the inner core) are likely to be formed in the free atmosphere, or in the outer part of the column, where rain droplets may be present.

According to the theoretical kernels for particle collisions in turbulent or sedimentation regimes[4,15], we expect a collision rate $\beta \propto (r_i + r_j)^2 \cdot \langle|\vec{u}_r|\rangle$, where r_i and r_j are the particle radii and $\vec{u}_r$ the relative radial velocity between the objects. This means that the collision rate of relatively large objects, such as PC3 and rain droplets (~200–1000 μm) that move with non-zero relative velocities is more than probable from a theoretical point of view. However, the fact that this work represents the first field-based evidence of cAP1 should stress how important is the use of cutting-edge techniques in modern field volcanology.

We suggest that the absence of a clear radial trend in the spatial distribution of density and porosity values in cAP1 and PC3 outer shells, clearly shown by Fig. 5, is a characteristic feature of these aggregates, as the net X-ray attenuation is likely to be conserved notwithstanding the already discussed limitations of the derived quantitative data. This suggests that the formation mechanisms of these aggregates are not expected to be gradual and related to the progressive passage through environments characterized by the presence of well size-sorted material.

Comparison of the various field strategies used to characterize volcanic ash aggregates

Since the eruption of Mt. St Helens in May 1980, volcanic ash aggregation started claiming a continuously growing attention by the scientific community due to its crucial role in affecting the atmospheric dispersal and ground sedimentation of volcanic ash[2,6,7,9,10,16,19,23,27,38,40–42]. Since then, various techniques were developed to characterize volcanic ash aggregates and to measure the associated physical parameters, all with specific advantages and limitations (Table 3).

One of the most recently developed strategies used to characterize volcanic ash aggregates is performed during deposition and includes the collection of aggregates on adhesive tapes for the analysis at the SEM combined with the analysis of their HR-HS video footages[8,9,18,20]. This strategy allows both for the classification of aggregates and for the

Table 3 | Summary of main existing strategies used to characterize volcanic ash aggregates collected in the field

Strategy	Main objectives	Main limitations
Analysis of tephra deposits	Identification of aggregates that have been preserved in the tephra deposits and/or interpretation of tephra sedimentation based on grainsize populations (e.g., unimodal vs polymodal distributions)	This analysis can only be applied to AP2s (i.e., Accretionary Lapilli) that are often preserved in tephra deposits. Polymodal grainsize distributions cannot be solely associated with aggregation processes.
SEM analysis of aggregates embedded with resin after sedimentation	Characterization of internal structure and porosity of aggregates.	This analysis can only be applied to AP2s (i.e., Accretionary Lapilli) that are often preserved in tephra deposits.
Collection of aggregates on adhesive tapes for analysis at the SEM	Characterization of the external morphometry and texture of aggregates. Internal grainsize is also possible in case of partial breakage of the aggregate.	The most fragile aggregates (i.e., PCs) generally do not preserve their airborne structure during the impact with SEM tape. The internal structures of un-broken aggregates cannot be determined.
HS-HR camera video analysis	Determination of aerodynamic parameters of ash aggregates (size, shape, terminal velocity, and bulk density).	Unless combined with the collection on adhesive tape, this strategy does not provide any direct information upon the internal structure of ash aggregates. In fact, the image quality is often too low to allow for a good recognition and identification of the aggregate type.
μCT analysis	Determination of high resolution and high-quality information on the external and internal structure of ash aggregates, including internal porosity network and internal layering. Possible quantification of bulk density and of density of single constituents.	The quality of CT data is related to the resolution of the μCT (instrument used here, approximately 4.2 μm), and to the possible occurrence of dark artifacts, likely caused by minimal sample motion during scanning. These factors, combined with the complex structure of aggregates, characterized by the presence of heterogeneous and polydisperse materials, represent major challenges influencing the uncertainty associated with the quantification of the physical parameters (such as density and grain size of aggregates constituents). Density calibration can partially mitigate the problem by reducing uncertainty.

determination of associated physical parameters (e.g., size, density, velocity). Limitations mostly include the preservation capability of aggregates, due to the extreme fragility of PCs and the inherent difficulty to preserve the entire particle assemblage (and in particular the coarser particles) and the limited optical resolution imposed by the complex field setup of HSC cameras[8,20] which often precludes a precise measurement of the aggregate size (and hence volume).

The innovative sampling and analytical strategy introduced in this work greatly increased the preservation potential of the different types of aggregates. We demonstrate that even the most fragile aggregates (PCs) can be preserved by means of a UV-light sensitive resin, capable of rapidly immobilizing both the external and internal structure of all 0 the aggregate types here analyzed. HR-HS videos of settling aggregates, acquired in synchro with the aggregate collection (see Section S2 of supplementary materials and Supplementary Movie 1 in the online repository) clearly demonstrated the efficiency of the collection strategy. In addition, the collected aggregates can be stored in small, resin-cured handy tubes and transported in the laboratory to perform X-ray micro-tomographic investigations without affecting the reliability of the sample. Porosity evaluation as well as the comparison between the architecture of the internal porosity network and the aggregates structure (Fig. 3) are also particularly useful when we consider the aerodynamic behavior and the boundary layer generated by the particle shape while falling, that results in a modified effective external shape and apparent density of falling aggregates. Such a characterization is crucial to an accurate quantitative parametrization of aggregate structure within numerical schemes.

Concluding remarks

In this work we presented the results of the study of volcanic ash aggregates based on a new methodology which couples an unbiased sampling technique with μCT analyses. This approach revealed features and complexities in the inner structures of the volcanic ash aggregates with a detail and accuracy never reached before on such a large range of different aggregate morphologies, giving the possibility to derive a set of physical data on the different aggregate types. This unique, cutting-edge technique specifically designed for volcanic ash aggregates represents the benchmark for future theoretical studies in this field, as it can be used to discuss some main important processes related to ash aggregation in volcanic clouds.

The observed morphological variability of ash aggregates is the base to discuss sedimentation processes. For example, more equant and low-roughness aggregates morphologies, like those observed for APs and PC2s, will generally result in a reduced atmospheric drag and higher terminal velocities compared to other PCs. The description of the aggregates' morphology is, therefore, key to the definition of their aerodynamic behavior and, therefore, to ash dispersal forecasting.

The complete description of external morphometry and inner structures of the main types of volcanic ash aggregates (PC1, PC2, PC3, AP1, AP3), and their association with external parameters (atmospheric conditions, plume height, etc.) are the key to discuss basic formation processes of the different types of aggregates. This new dataset represents an important step forward that also integrates previous studies based on more simplified sampling and analytical techniques[2,7–9,20,31].

The high preservation potential of the adopted sampling technique is fundamental for the recognition of some particularly fragile aggregates. We report the first observations of poorly structured, sub-spherical pellets, presenting one or more large particles acting as a core (defined as cored-AP1: cAP1). The occurrence of the cAP1s in the fallout is strongly related to rainy weather conditions, suggesting an aggregation mechanism controlled by the interaction between PC3 aggregates with water droplets.

The proposed methodology can produce high resolution images of the inner regions of all the aggregate types reported in the literature. The interior of aggregates provides fundamental insights into their genesis: their formation, the population of particles encountered along its path, the sticking mechanisms, the leading collisional kernels as a function of time, the number of collisions, the density. The dataset thus represents a unique benchmark for all those studies that aim to better characterize the theoretical description of the ash particles collisional and sticking processes[4], and a calibration for all those works that investigate the packing of volcanic ash and its consequence on sedimentation[12,13,43].

For the first time, we have access to the hidden side of ash aggregation for a large variety of aggregate types, as it occurs in nature, without any alteration of the original structure.

Methods

Aggregate sampling strategy

A total of 51 natural volcanic ash aggregates including different types of both Particle Clusters (PCs) and Ash Pellets (APs) were collected at Sakurajima volcano (Japan) during several pulses of cyclic, high-frequency and ash-dominated Vulcanian activity occurred in the period from 17 to 26 November 2019 (see Table 1).

Analyzed aggregates were collected during tephra fallout by means of a state-of-the-art sampling strategy in which a dedicated glass support, posed in the field of view of a High-Speed, High-Resolution Phantom Pro camera (HS-HRC), is coated with a thick layer of UV-sensitive epoxy resin and later exposed for a short amount of time (~ 10 s) to the ash fallout. The HS-HSC was equipped with a Nikon 60 mm f/2.8D AF Micro Nikkor lens. Falling aggregates were filmed during their impact into the resin in order to verify the occurrence of eventual structural modifications. Finally, the resin and the embedded aggregates were cured in a few seconds with the use of a UV-light lamp, resulting in a solid shell that preserved the shape of the aggregates during transport from field to lab. This sampling strategy has shown to fully preserve the airborne structure of even the most fragile Particle Clusters (PCs), preventing the original structure to be disaggregated at the impact with the sampling support (Supplementary Movie 1: HS-HRC video of falling aggregates reported in the on-line repository and detailed in supplementary materials S2).

The meteorological conditions during the whole period of data collection were monitored using a portable meteorological station (Kestrel 5500 weather station) and the main physical parameters are reported in Table 1 (see also ref. 20 for details about sample locations).

Micro-CT tomography setup

Two samples of each aggregate category as defined by refs. 2, 9 (i.e., PC1, PC2, PC3, AP1, AP2, AP3) were selected to be analyzed by means of the Bruker SkyScan 1273 X-Ray µCT of the University of Lausanne, Institute of Earth Sciences (ISTE) (Switzerland) (see Section S3 of the supplementary materials). The X-Ray images of the aggregates were collected directly mounting the resin coated samples on a dedicated 4 mm wide brass support. A fixed analytical setup was used for the analysis of the entire sample set (e.g., source voltage = 50 kV; source current = 100 µA; 1674 ms of exposure time; angle step = 0.125). For a given aggregate, analysis resulted in a set of thousands raw images consisting in the 2D angular projections along the x-y plane over 360° degrees (see Fig. 1). The final 3D tomography reconstruction along the *z* axis was then obtained by using the SkyScan *NRecon* software[44]. The setup used in the analysis allowed us to reach a constant Image Resolution (IR) of 4.2 µm per pixel corresponding, in the reconstructed tomographies, to a cubic voxel size of $4.2 \times 4.2 \times 4.2\ \mu m^3$.

Greyscale calibration for the estimation of aggregate density

In the reconstructed tomographic images, the µCT associates a gray-scale value to each 3D cubic voxel ($4.2\ \mu m^3$ in size). The setup adopted during the X-ray scanning resulted in a fixed dependency between the greyscale color of a single voxel and the actual density of the material enclosed within that voxel (i.e., the Bulk Voxel Density). In particular, the gray level depends on beam attenuation, resulting in the intensity measured on a variety of rotation angles (see methods for further details, see also ref. 45 and visit https://www.ctlab.geo.utexas.edu). In order to associate the gray-scale value of each voxel to a specific density value, a specific calibration was performed using a dataset of homogeneous and not porous specimens that were selected as reference materials and therefore used to estimate the effective density of each voxel in the aggregates (Table 4).

The density of each reference material was measured using a water pycnometer obtaining a list of values that span from about 0.001 g/cm^3 (air) to 5 g/cm^3 (titanium) (Table 4). This density range was selected to reasonably cover the expected density of ash and crystal components which are normally found in volcanic ash at Sakurajima volcano (e.g., ref. 33). The different materials were then X-ray scanned with the µCT using the same setup adopted for the aggregates. Finally, the reconstructed 3D tomographic images were processed using Fiji software to obtain the greyscale distribution of the voxels that characterize each specimen (Fig. 6).

Table 4 | List of the selected materials used as a reference for the greyscale calibration of the aggregate tomography

Reference materials	Measured density (g/cm^3)	Mode Greyscale value	16th Perc Greyscale value	84th Perc Greyscale value
AirBubble	0	0	0	1
Alluminium	2.71	89	85	91
Hydrogen Borate	1.44	16	8	21
Pure UV Resin	1.1	12	10	13
Glass Bead	2.5	83	79	87
MgOlivine	3.3	109	104	114
Sanidine	2.5	81	77	85
Titanium	4.5	255	254	255

Information about the associated greyscale colors of each material (statistical descriptors) is reported together with their density values measured using a water pycnometer. The 16th and 84th percentile correspond to the values of the grey-scale distribution corresponding respectively to the 16% and 84% of curve integral.

The mode of each voxel's distribution was selected to represent the characteristic greyscale for each material listed in Table 2, together with a 2-sigma interval of confidence (16° and 84° percentiles). The mathematical relationship that relates the grey-scale values of the known materials to their density has been found by means of a power-law fitting (Fig. 7):

$$\rho_{vox} = b \cdot g_{vox}^{m} \quad (1)$$

where ρ_{vox} is the bulk density of a voxel, g_{vox} is the voxel greyscale, and the fitting coefficients are respectively $b = 0.3786$ and $m = 0.4466$. It is worth noticing that titanium was not considered in the fitting curve due to its high degree of saturation in the raw images.

3D image processing

We created a dedicated software that combines MATLAB and Fiji[46] to process the raw dataset of images resulted from the X-ray scanning of the collected aggregates. The algorithm (Fig. 8) was implemented to reconstruct 3D images starting from the 2D projections and to derive the main physical parameters of the aggregates.

The procedure is described as follows. Initially, the slices acquired on the x-y plane after a complete 360° degrees µCT analysis (see the X-ray slice reported in the inset for image quality check) were vertically aligned to produce a greyscale volumetric image of the aggregate (Fig. 8a). Each reconstructed tomography was then processed using Fiji to characterize the greyscale distribution of the resin in which the aggregate was embedded. In this step we analyzed the variability of the voxels' greyscale associated with the resin to identify possible artifacts that can occasionally affect the resin in the vicinity of the aggregate boundaries. Then, different grey-scale thresholds were defined to perform the 3D segmentation of the tomography (Fig. 9b). This allowed us to obtain several indexed volumetric images that could be later used to extract information about the aggregate morphology and the internal structure.

The first grey-scale threshold is set corresponding to the upper limit of the resin greyscale distribution and used to segment the aggregate from the surrounding resin. The indexed greyscale image resulting from this process defines the set of xyz coordinates and the grey values of the voxels forming the aggregate (Fig. 8c), and allowed the calculation of several physical parameters. In particular, the bulk volume of the aggregate was calculated considering the cumulative volume of the voxels included in this indexed image. The density of the aggregate was computed as the average density of all the voxels that define the aggregate in the volumetric image, by iterating the greyscale-to-density function over all the voxels of the indexed image

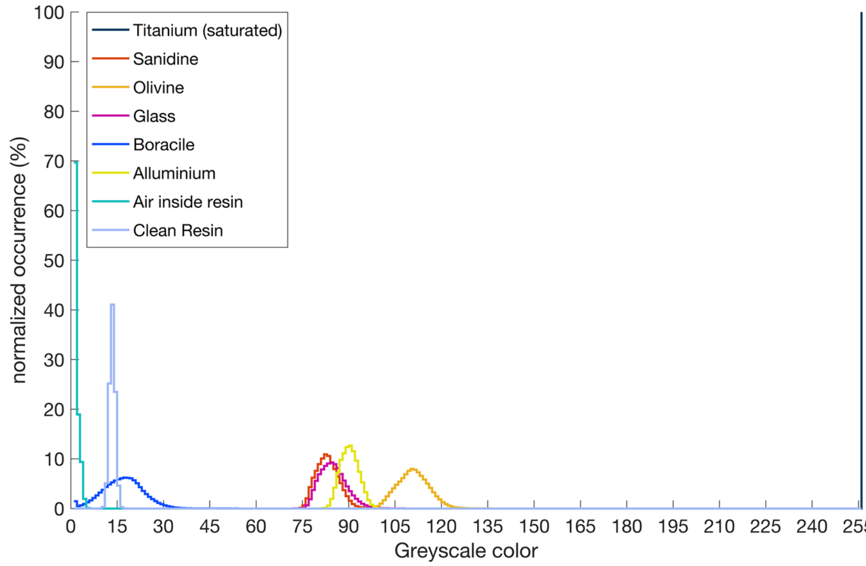

Fig. 6 | Color characterization of the materials used to calibrate microCT results. Frequency distributions of the voxels greyscale colors for different materials used as a reference for the color scale calibration.

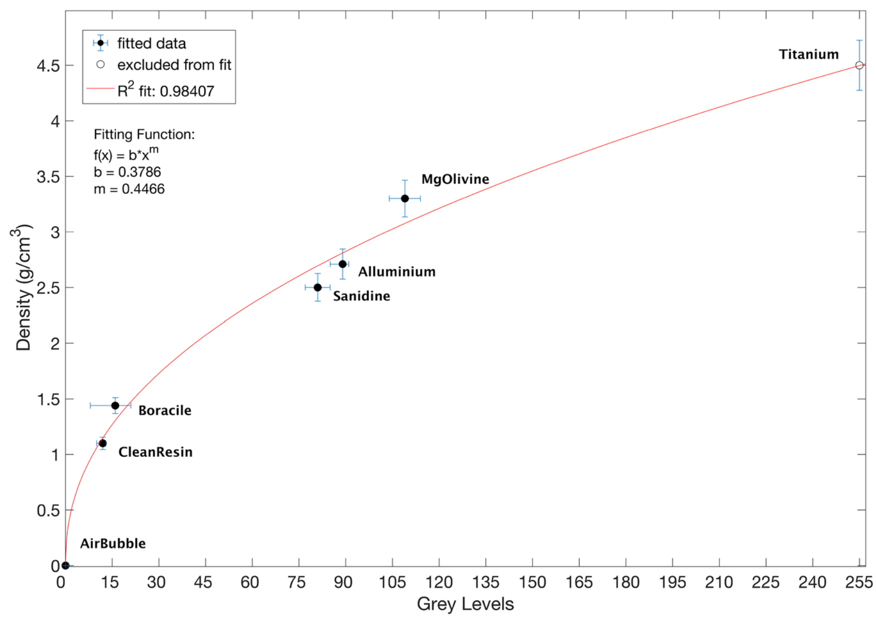

Fig. 7 | Power-law fitting of the bulk densities of known materials as a function of the greyscale color of the voxels. In the top-left corner the fitting parameters are reported. Although reported in the plot and perfectly matching the fitting function, titanium (void circle) is not considered in the point fitting calculation since its grey-scale distribution was saturated.

also including voxels belonging to the internal aggregate porosity network, which are considered having zero density. The aggregate size was measured as the diameter of the sphere having equivalent volume, while the size of its internal core, where present, was estimated considering the best approximating cross-cutting slice of the tomography. Finally, a movie of the rotating 3D aggregate was produced and stored in the on-line repository (see Supplementary Movie 2 in the on-line repository).

Though the reconstruction of the bulk volume of the aggregate is straightforward thanks to the large density contrast existing between the embedding resin and the sample, the reconstruction of the internal part of the aggregate is much more complex due to the presence of different internal constituents (volcanic glass and minerals) having similar density. The criterion applied to visualize the inner structure is based on the definition of three density intervals: *low-density components* (1.9–3 g/cm^3), *mid-density components* (3–4 g/cm^3) and *high-density components* (>4 g/cm^3) (see Fig. 8c). These density intervals were chosen to correspond respectively to the typical density range of: (i) volcanic glass and feldspars, (ii) Mg-Olivine, and (iii) Fe-Ti Oxides, which are the typical components found in the ash from Sakurajima[33,37,47–49]. The internal regions of the aggregates were reconstructed as the set of greyscale voxels matching a given density interval, selected according to the calibration procedure, and obtained thus a model in which different iso-density levels are highlighted. This technique allowed the visualization of the spatial arrangement of the aggregate internal constituents, and the quantification their cumulative volume, density, and mass. Information on density of constituents were also used to determine the position of both the geometrical and the mass centroids of the aggregate. A dedicated video of the slice-by-slice segmentation procedure is reported in the online repository (see Supplementary Movie 3 in the on-line repository).

The study of the overall porosity of the aggregate requires a dedicated threshold, which is defined as the voxel value corresponding to the 50° percentile of the greyscale distribution of the resin affected by dark artifacts. The threshold represents the best compromise of analysis and it set assuming that no or very few UV resin permeated inside the internal structure of the aggregates, since only ~10 s elapsed between the aggregate landing and the resin curing. According to this, the porosity is then estimated as the sum of the voxels with grey value below this threshold.

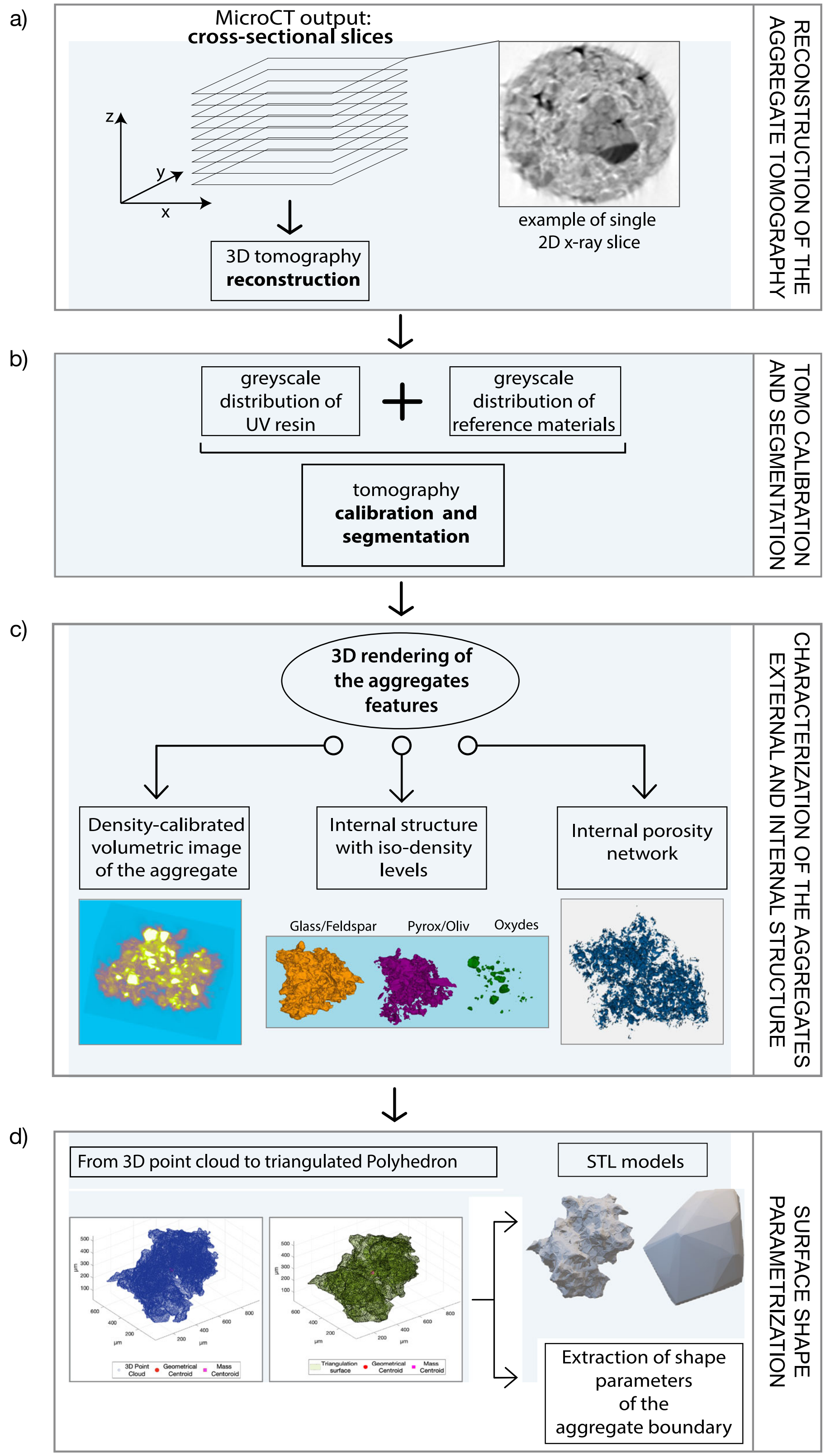

Fig. 8 | Flow-chart of the algorithm designed to analyze the μCT data, with the outlined macro steps (color boxes). a the reconstruction of the aggregate tomography starting from the stack of 2D x-ray slices; **b** Greyscale characterization of the UV resin and the reference materials in order to perform a density calibration of the microCT results; **c** 3D rendering of the different aggregates features to visualize the density distribution of the internal components, the geometry and volume fraction of iso-density levels and architecture of the porosity network; **d** 3D mesh and STL models representing the approximated external aggregates morphology resulted from point clouds triangulation.

Considering the coordinates of the voxels with a grey-scale index below this threshold, this procedure allows us to visualize the three-dimensional spatial distribution of pores inside the aggregates. Similarly, the porosity and its spatial distribution can be estimated also for the external shell of aggregates, in the case of aggregate types showing a structure characterized by the presence of an internal core (PC3 and cAP1).

Finally, the voxels comprised in the volumetric image of the aggregate were treated as a 3D point cloud to produce a triangulated surface of the external boundary (Fig. 8d). Each aggregate can be thus represented as a complex solid polyhedron using the MATLAB built-in function *alpha-Shape*, that uses a Delaunay triangulation and a dedicated *alpha-radius* to connect the external vertexes with a variable degree of approximation for the

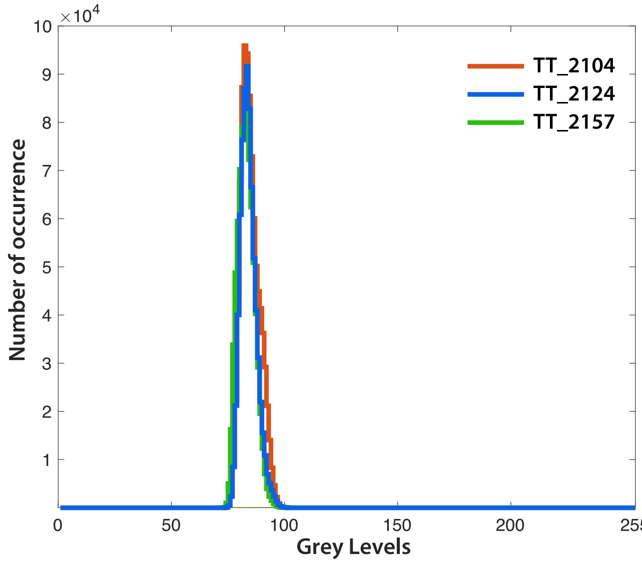

Fig. 9 | Greyscale distribution of the voxels associated with the repeated analysis of the same sample. Colors indicate the distribution associated with the first (TT_2104), the second (TT_2124) and third (TT_2157) repetition.

non-convex regions. Among all the possible alpha-radii, two triangulated surfaces are finally selected to describe the minimum and the maximum volumes compatible with the 3D point cloud of the object, corresponding respectively to the tightest alpha shape and to the convex hull (minimum convex polyhedron enveloping the shape). These two polyhedrons represent the end-members that can be used as proxies to calculate fundamental shape descriptors, such as Solidity (volume of the particle surface to the volume of its convex hull), Convexity (surface extent of the convex hull to the surface extent of the aggregate), Sphericity (defined as the ratio of the surface area of the sphere with the same volume as the given aggregate to its surface area), and to the external Surface Roughness (defined as the relative difference between the volume of the convex hull and the volume of the tightest alpha shape of the aggregate to the volume of aggregate convex hull). All these 3D shape parameters are defined according to refs. 50–52; see Section S5 of supplementary materials for further information.

A remarkable aspect of the designed procedure is the possibility to compute the stereo lithography model of the aggregate (e.g., the STL file), which is based on the tightest alpha shape representation of the triangulation, which closely follow the real aggregate boundary. STL files allow for the 3D printing of the aggregate or its inner parts, defined by the previously mentioned thresholds. The STL files of the aggregates analyzed in the present work can be found in the online repository (see.STL files in the online repository).

Uncertainties and validation

Stability of the setup and reproducibility of the results. The micro-CT scanning setup was kept constant during the whole scanning session, both for the aggregates and the reference materials. However, a certain variability in the results can always occur due to random drifts in the support and the sample. This can introduce biases or artefacts in the final results. In order to test the effective stability of the setup, we used a fixed sample as a benchmark and we repeated the micro-CT scanning of the object at the beginning (TT_2104), in an intermediate (TT_2124) stage and at the end (TT_2157) of each daily session. The resulting images were aligned and reconstructed using the NRecon software in order to produce three replicated volumetric images of the benchmark. The greyscale distribution of the voxels was computed and compared for all the repetitions (Fig. 9). The comparison between these distributions clearly shows a high degree of stability in the setup and an almost perfect matching among the three replicated analyses.

Volume and density evaluation. The accuracy on the evaluation of volume and density of aggregate and their internal constituents was tested using a calibration glass-bead with a known volume ($V_{GB} \sim 0.0082\ mm^3$) and density ($\rho_{GB} \sim 2.5\ g/cm^3$). The glass-bead was mounted on the same support used during the analysis of all the samples and scanned with the same standard procedure designed for the aggregates (e.g., Eq. 1 for the grey-scale to density calibration). The measured volume of the glass-bead ($V_{GB\_m} = 0.0086\ mm^3$) resulted to be overestimated by about 4.8% respect to the reference value, while the measured density ($\rho_{GBm} = 2.79\ g/cm^3$) was overestimated by about 10%.

This test indicates a good agreement between the theoretical and the measured volumes and densities.

Though uncertainty related to density estimation of large objects yields good results, the calculation of density associated to natural volcanic aggregates implies other source of errors like the presence of dark artifacts affecting in a variable degree of intensity the different aggregates and their internal constituents. In order to account for this issue, for each aggregate, we measured the voxels greyscale distribution of the resin affected by dark artifacts, and considering the greyscale level corresponding to the 16th and 84th percentiles of the voxel distribution we defined a minimum and maximum value of bulk density for the aggregates.

Estimation of the aggregate porosity. Aggregate porosity results from the ratio between the total volume of voxels considered as voids (e.g., grey level below the 50th percentile of the resin distribution affected by dark artifacts), and the total volume of the aggregate. Since porosity estimations can be viewed as a ratio between volumes, we can affirm that the good results obtained for the volumes estimation, in particular for large particles, will result in good estimations also for aggregate volume. The uncertainty associated to the volume of aggregate internal voids was instead evaluated considering segmented volumes resulting from two thresholds corresponding respectively to the 16th and 84th percentiles of voxel values from the resin affected by dark artifacts. This provided estimates for both minimum and maximum porosity.

Greyscale artifacts affecting the resin. A probable source of uncertainty, during the segmentation process, is due to the presence of dark artifacts that contaminates the true grey color of voxels in the tomographies (see Section S6). These artifacts are possibly caused by slight misalignments of the raw 2D slices of tomographies resulting in geometric reconstruction errors. This is possibly due to minimal sample movements during X-ray scanning caused by modifications experienced by the plasteline used to fix the sample to the sample carrier during prolonged X-Ray exposure. Their presence is promoted by the very fine-grained nature of ash aggregates which push the analysis very close to the resolution limit of the instrumental setup. The abundancy and intensity of altering flares is certainly enhanced by the complex nature of the investigated samples, since they consist of non-homogeneous materials with highly variable density and lithology, characterized by complex geometries and sharp boundaries between the inner particles.

This significant source of error was taken into account in the procedure, by performing an ad-hoc statistical evaluation and acquisition of the grey-scale levels that defines the resin. For each sample, we identified a representative set of voxels where only resin is present, and we computed two different grey-scale distributions: a first distribution of pure resin not affected by dark spurious colors and a second distribution of resin contaminated by dark flares due to the artifacts. Both the distributions were considered in the definition of the thresholding levels used to account for possible uncertainties due to the presence of dark artifacts in the aggregate perimeter and in the contours of their internal iso-density levels.

Despite the ad-hoc procedure useful to mitigate the altering effect of these artifacts, we cannot exclude they could affect results of quantification, potentially leading to the overestimation of aggregates density and underestimation of their porosity.

In particular, the most affected aggregates categories are those exhibiting more complex geometries and finer components, and hence PC1 and PC3. On the other hand, we consider PC2 and other APs as reasonably the least affected by the problem.

Sub-voxel resolution. The tomography analysis produces a greyscale image in which the intensity of each voxel is a function of the bulk density and the chemistry of the material within the voxel. However, μCT averages whatever is smaller than the voxel resolution (i.e., $4.2 \times 4.2 \times 4.2\ \mu m^3$). This lack of smaller resolutions is the principal source of uncertainty when the size of the scanned objects is smaller than the pixel size (e.g., very fine grained and heterogeneous particles). In order to consider this source of error, we followed a precautionary approach in which we varied the percentiles of the grey-scale distributions to finally produce minimum and maximum values of all the estimated quantities.

SEM analysis

Since μCT allows a non-destructive analysis of the samples, a selected set of embedded aggregates was used to collect SEM images to better resolve and describe internal structures. sThe resin coated aggregates were sectioned, polished and carbon coated in order to be reanalyzed with SEM using the back-scattered electrons mode (BSE-SEM) to obtain images representative of the internal characteristics of the aggregates.

Data availability

All the raw data used in this study are reported in the tables of included in main text and supplementary information.

Received: 5 March 2024; Accepted: 13 May 2025;
Published online: 03 July 2025

References

1. Durant, A. J. RESEARCH FOCUS: toward a realistic formulation of fine-ash lifetime in volcanic clouds. *Geology* **43**, 271–272 (2015).
2. Brown, R. J., Bonadonna, C. & Durant, A. J. A review of volcanic ash aggregation. *Phys. Chem. Earth, Parts A/B/C.* **45**, 65–78 (2012).
3. Van Eaton, A. R. & Wilson, C. J. The nature, origins and distribution of ash aggregates in a large-scale wet eruption deposit: Oruanui, New Zealand. *J. Volcanol. Geotherm. Res.* **250**, 129–154 (2013).
4. Costa, A., Folch, A. & Macedonio, G. A model for wet aggregation of ash particles in volcanic plumes and clouds: 1. Theoretical formulation. *J. Geophys. Res.: Solid Earth*, **115**, https://doi.org/10.1029/2009JB007175 (2010).
5. Rose, W. I. & Durant, A. J. Fate of volcanic ash: aggregation and fallout. *Geology* **39**, 895–896 (2011).
6. James, M. R., Lane, S. J. & Gilbert, J. S. Density, construction, and drag coefficient of electrostatic volcanic ash aggregates. *J. Geophys. Res.: Solid Earth* **108**, https://doi.org/10.1029/2002JB002011 (2003).
7. Taddeucci, J. et al. Aggregation-dominated ash settling from the Eyjafjallajökull volcanic cloud illuminated by field and laboratory high-speed imaging. *Geology* **39**, 891–894 (2011).
8. Gabellini, P. et al. Physical and aerodynamic characterization of particle clusters at Sakurajima volcano (Japan). *Front. Earth Sci*. **8**, 575874 (2020).
9. Bagheri, G., Rossi, E., Biass, S. & Bonadonna, C. Timing and nature of volcanic particle clusters based on field and numerical investigations. *J. Volcanol. Geotherm. Res.* **327**, 520–530 (2016).
10. Carey, S. N. & Sigurdsson, H. Influence of particle aggregation on deposition of distal tephra from the May 18, 1980, eruption of Mount St-Helens volcano. *J. Geophys. Res.* **87**, 7061–7072 (1982).
11. James, M. R., Gilbert, J. S. & Lane, S. J. Experimental investigation of volcanic particle aggregation in the absence of a liquid phase. *J. Geophys. Res.: Solid Earth* **107**, ECV–4 (2002).
12. Rossi, E., Bagheri, G., Beckett, F. & Bonadonna, C. The fate of volcanic ash: premature or delayed sedimentation?. *Nat. Commun.* **12**, 1303 (2021).
13. Beckett, F., Rossi, E., Devenish, B., Witham, C. & Bonadonna, C. Modelling the size distribution of aggregated volcanic ash and implications for operational atmospheric dispersion modelling. *Atmos. Chem. Phys.* **22**, 3409–3431 (2022).
14. Veitch, G. & Woods, A. W. Particle aggregation in volcanic eruption columns. *J. Geophys. Res.: Solid Earth* **106**, 26425–26441 (2001).
15. Textor, C. et al. Volcanic particle aggregation in explosive eruption columns. Part I: parameterization of the microphysics of hydrometeors and ash. *J. Volcanol. Geotherm. Res.* **150**, 359–377 (2006).
16. Durant, A. J., Rose, W. I., Sarna-Wojcicki, A. M., Carey, S. & Volentik, A. C. M. Hydrometeor-enhanced tephra sedimentation: constraints from the 18 May 1980 eruption of Mount St. Helens. *J. Geophys. Res. Solid Earth* **114**, https://doi.org/10.1029/2008JB005756 (2009).
17. Bonadonna, C. et al. *Tephra Fallout in the Eruption of Soufrière Hills* (Volcano, Montserrat, 2002).
18. Bonadonna, C. et al. Tephra sedimentation during the 2010 Eyjafjallajökull eruption (Iceland) from deposit, radar, and satellite observations. *J. Geophys. Res.: Solid Earth*, **116** (2011).
19. Miwa, T., Iriyama, Y., Nagai, M. & Nanayama, F. Sedimentation process of ashfall during a Vulcanian eruption as revealed by high-temporal-resolution grain size analysis and high-speed camera imaging. *Prog. Earth Planet. Sci.* **7**, 1–16 (2020).
20. Vecino, M. C. D. et al. Aerodynamic characteristics and genesis of aggregates at Sakurajima Volcano, Japan. *Sci. Rep.* **12**, 2044 (2022).
21. Mueller, S. B. et al. Ash aggregation enhanced by deposition and redistribution of salt on the surface of volcanic ash in eruption plumes. *Sci. Rep.* **7**, 45762 (2017).
22. Moore, J. G. & Peck, D. L. Accretionary lapilli in volcanic rocks of the western continental United States. *J. Geol.* **70**, 182–193 (1962).
23. Gilbert, J. S. & Lane, S. J. The origin of accretionary lapilli. *Bull. Volcanol.* **56**, 398–411 (1994).
24. Schumacher, R. & Schmincke, H. U. Models for the origin of accretionary lapilli. *Bull. Volcanol.* **56**, 626–639 (1995).
25. Mueller, S. B., Kueppers, U., Ayris, P. M., Jacob, M. & Dingwell, D. B. Experimental volcanic ash aggregation: internal structuring of accretionary lapilli and the role of liquid bonding. *Earth Planet. Sci. Lett.* **433**, 232–240 (2016).
26. Morgavi, D. et al. Volcanic ash aggregation enhanced by seawater interactions: the case of the "Secche di Lazzaro phreatomagmatic deposit (Stromboli). *Ann. Geophys.* **61** (2018).
27. Burns, F. A., Bonadonna, C., Pioli, L., Cole, P. D. & Stinton, A. Ash aggregation during the 11 February 2010 partial dome collapse of the Soufrière Hills Volcano, Montserrat. *J. Volcanol. Geotherm. Res.* **335**, 92–112 (2017).
28. Orhan, K. (ed). *Micro-Computed Tomography (micro-CT) in Medicine and Engineering (No. 179941)* (Springer, Berlin/Heidelberg, Germany, 2020).
29. Ketcham, R. A. Three-dimensional grain fabric measurements using high-resolution X-ray computed tomography. *J. Struct. Geol.* **27**, 1217–1228 (2005).
30. Vonlanthen, P. et al. High-resolution 3D analyses of the shape and internal constituents of small volcanic ash particles: the contribution of SEM micro-computed tomography (SEM micro-CT). *J. Volcano. Geotherm. Res* **293**, 1–12 (2015).
31. Takishita, K., Poulidis, A. P. & Iguchi, M. In-situ measurement of tephra deposit load based on a disdrometer network at Sakurajima volcano, Japan. *J. Volcanol. Geotherm. Res.* **421**, 107442 (2022).
32. Iguchi, M., Yakiwara, H., Tameguri, T., Hendrasto, M. & Hirabayashi, J. I. Mechanism of explosive eruption revealed by geophysical observations at the Sakurajima, Suwanosejima and Semeru volcanoes. *J. Volcanol. Geotherm. Res.* **178**, 1–9 (2008).

33. Miwa, T., Geshi, N. & Shinohara, H. Temporal variation in volcanic ash texture during a vulcanian eruption at the Sakurajima volcano, Japan. *J. Volcanol. Geotherm. Res.* **260**, 80–89 (2013).
34. James, M. R., Lane, S. J. & Gilbert, J. S. Volcanic plume electrification: experimental investigation of a fracture-charging mechanism. *J. Geophys. Res.: Solid Earth* **105**, 16641–16649 (2000).
35. James, M. R. et al. Electrical charging of volcanic plumes. *Space Sci. Rev.* **137**, 399–418 (2008).
36. Méndez Harper, J. & Dufek, J. The effects of dynamics on the triboelectrification of volcanic ash. *J. Geophys. Res.: Atmospheres* **121**, 8209–8228 (2016).
37. Gabellini, P. et al. Eruptive dynamics and fragmentation mechanisms during cyclic Vulcanian activity at Sakurajima volcano (Japan): insights from ash texture analysis. *J. Volcanol. Geotherm. Res.* **428**, 107582 (2022).
38. Sorem, R. K. Volcanic ash clusters: tephra rafts and scavengers. *J. Volcanol. Geotherm. Res.* **13**, 63–71 (1982).
39. Hoult, H. et al. Growth of complex volcanic ash aggregates in the Tierra Blanca Joven eruption of Ilopango Caldera, El Salvador. *J. Volcanol. Geotherm. Res.* **431**, 107670 (2022).
40. Cornell, W., Carey, S. & Sigurdsson, H. Computer-simulation of transport and deposition of the Campanian Y-5 Ash. *J. Volcanol. Geotherm. Res.* **17**, 89–109 (1983).
41. Schumacher, R. A reappraisal of Mount St-Helens ash clusters - depositional model from experimental-observation. *J. Volcanol. Geotherm. Res.* **59**, 253–260 (1994).
42. Bonadonna, C., Macedonio, G. & Sparks, R. S. J. *Numerical Modelling of Tephra Fallout Associated with Dome Collapses and Vulcanian Explosions: Application to Hazard Assessment on Montserrat*. Vol. **21**, 517–537 (Geological Society, London, Memoirs, 2002).
43. Rossi, E. & Bonadonna, C. SCARLET-1.0: SpheriCal approximation for viRtuaL aggrEgaTes. *Geosci. Model Dev.* **14**, 4379–4400 (2021).
44. Liu, X. & Sasov, A. Cluster reconstruction strategies for microCT/nanoCT scanners. In *Proc. Fully 3D Image Reconstruction Meeting in Radiology and Nuclear Medicine* 215–218 (2005).
45. Roth, A. S. G., Metzler, K., Baumgartner, L. P. & Leya, I. Cosmic ray exposure ages of chondrules. *Meteorit. Planet. Sci.* **51**, 1256–1267 (2016).
46. Schindelin, J. et al. Fiji: an open-source platform for biological-image analysis. *Nat. Methods* **9**, 676–682 (2012).
47. Yamanoi, Y., Takeuchi, S., Okumura, S., Nakashima, S. & Yokoyama, T. Color measurements of volcanic ash deposits from three different styles of summit activity at Sakurajima volcano, Japan: conduit processes recorded in color of volcanic ash. *J. Volcanol. Geotherm. Res.* **178**, 81–93 (2008).
48. Miwa, T., Toramaru, A. & Iguchi, M. Correlations of volcanic ash texture with explosion earthquakes from vulcanian eruptions at Sakurajima volcano, Japan. *J. Volcanol. Geotherm. Res.* **184**, 473–486 (2009).
49. Miwa, T., Shimano, T. & Nishimura, T. Characterization of the luminance and shape of ash particles at Sakurajima volcano, Japan, using CCD camera images. *Bull. Volcanol.* **77**, 1–13 (2015).
50. Wadell, H. Volume, shape, and roundness of rock particles. *J. Geol.* **40**, 443–451 (1932).
51. Zhao, B. & Wang, J. 3D quantitative shape analysis on form, roundness, and compactness with μCT. *Powder Technol.* **291**, 262–275 (2016).
52. Russ, J. C. *The Image Processing Handbook* (CRC Press, 2006).

Acknowledgements
the authors are grateful to Allan Fries, Jonathan Lemus, Stefano Pollastri, Alex Poulidis Valentin Freret-Lorgeril and Carolina Vecino for their support and discussion in the field. We also thank Benita Putlitz for her assistance in the laboratory of the University of Lausanne. This research was support by the Swiss National Science Foundation (grant numbers 200021_156255 and 200020_204315) and by the National Recovery and Resilience Plan—Mission 4 Component 2—Investment 1.3—PE0000005 RETURN—funded by the European Union—NextGenerationEU - CUP B83C22004820002. We specific that sample collection did not conflicts with any restriction.

Author contributions
P.G. and E.R. carried out the field sampling and the laboratory analysis of the aggregates and developed the post-processing strategy under the supervision of C.B., R.C. and L.B., P.G. and E.R. prepared the first draft of the manuscript. All authors, including M.P, were involved in the interpretation of the results and in the finalization of the manuscript.

Competing interests
The authors declare no competing interests.

Additional information
Supplementary information The online version contains supplementary material available at https://doi.org/10.1038/s43247-025-02378-y.

Correspondence and requests for materials should be addressed to Pietro Gabellini.

Peer review information *Communications Earth & Environment* thanks Richard Ketcham, Alastair Hodgetts and the other, anonymous, reviewer(s) for their contribution to the peer review of this work. Primary Handling Editor: Carolina Ortiz Guerrero. A peer review file is available